# Solid-state 3D micro-supercapacitors based on ionogel electrolyte: Influence of adding lithium and sodium salts to the ionic liquid

Thibaud Guillemin, Camille Douard, Kévin Robert, Bouchra Asbani, Christophe Lethien, Thierry Brousse, Jean Le Bideau

Version of Record: https://www.sciencedirect.com/science/article/pii/S2405829722002926
Manuscript_36e8cdeb74bbe139b356edfc5df4378d

## Title

Solid-state 3D micro-supercapacitors based on ionogel electrolyte: Influence of adding lithium and sodium salts to the ionic liquid

## Authors

Thibaud GUILLEMIN[1,2], Camille DOUARD[1,2], Kévin ROBERT[2,3], Bouchra ASBANI[2,3], Christophe LETHIEN[2,3,4], Thierry BROUSSE[1,2] and Jean LE BIDEAU[1,2]

*1. Université de Nantes, CNRS, Institut des Matériaux Jean Rouxel, IMN, 44000 Nantes, France*

*2. Réseau sur le stockage électrochimique de l'énergie (RS2E), CNRS FR3459, 80039, Amiens, France*

*3. Institut d'électronique de microélectronique et de nanotechnologie (IEMN), Université de Lille, CNRS, Centrale Lille, Université Polytechnique Hauts-de-France, UMR 8520 - IEMN, 59000 Lille, France*

*4. Institut Universitaire de France (IUF), France*

## Corresponding authors

Jean LE BIDEAU, jean.lebideau@cnrs-imn.fr

Thierry BROUSSE, thierry.brousse@cnrs-imn.fr

Christophe LETHIEN, christophe.lethien@univ-lille.fr

# Solid-state 3D micro-supercapacitors based on ionogel electrolyte: Influence of adding lithium and sodium salts to the ionic liquid

**Keywords (max 6)**

Micro-supercapacitor, 3D electrodes, solid-state device, ionogel, $MnO_2$, pseudocapacitance

**Abstract**

The ever-increasing interest in miniaturized Internet of Things devices and embedded electronics has given rise to a host of inquiries surrounding the need for safe, high performance energy storage devices. Solid-state 3D micro-supercapacitors based on ionogels provide a promising response to many of these pressing questions. Herein, leakage-free solid-state-like 3D micro-supercapacitors incorporating lithium and sodium salts added to 1-Ethyl-3-methylimidazolium bis(trifluoromethanesulfonyl)imide-based ionogels were investigated. The resulting micro-supercapacitors containing these lithium and sodium ions displayed energy densities of 10.2 and 9.5 $\mu Wh.cm^{-2}$ at power densities of 1.1 and 1.0 $mW.cm^{-2}$, respectively. In those devoid of these alkaline ions, however, the energy density reached a mere 3 $\mu Wh.cm^{-2}$ at the same power density, thereby validating the proposed strategy. The 3D interdigitated $MnO_2$ // $MnO_2$ micro-supercapacitors were cycled 50 000 times at 1.75 $mA.cm^{-2}$ with good capacitance retention (~ 85 %). While performing under high temperatures (100 °C), there was no evidence of electrolyte degradation, capacitance fading or electrolyte leakage.

## 1. Introduction

The Internet of Things (IoT) is a revolutionary technology aimed at streamlining the connection and communication between machines and devices. These chiefly include internet servers, personal computers, smartphones and, most notably, sensors [1], which are required to be autonomous and miniaturized. Several energy harvesting and scavenging technologies are currently being investigated as a means of supplying the energy required by these sensors [2–4], and since these energy sources are often intermittent, energy storage is critical when it comes to ensuring a stable power supply for electronic devices.

A viable approach to fulfilling this requirement involves the miniaturization of electrochemical energy storage systems (EESSs). Since the use of liquid electrolytes occasions packaging and safety issues [5], solid electrolytes are preferred. Polymer electrolytes were thus developed for use in all-solid-state lithium or Li-ion micro-batteries (µBats) [6]. These, however, display limited performance due to their planar configuration, having thereby led to current studies centered on µBats with 3D electrodes [7,8].

µBats can deliver a constant power supply for several hours, although such faradic devices show limited power capability and cycle life. In this context, therefore, if micro-supercapacitors (µSCs) were to be combined with µBats then the requirements for sustaining power pulses, together with steady energy delivery while providing high cycling stability, would simultaneously be met.

Indeed, µSCs have a long lifespan and are able to provide high power density due to the capacitive charge storage within the electrical double-layer capacitance [9]. On account of this, the performance of µSCs is greatly dependent upon the surface of the

electrodes, for which the planar configuration used for µBats is not feasible. There are two main options that are currently being considered for use as electrode materials in µSCs in order to improve their energy density: the first one entails using ultra-porous nano-engineered carbon materials, whereas the second one makes use of 3D electrodes [10]. In both cases, the use of pseudocapacitive materials is also an effective means of improving µSC performance. Pseudocapacitance refers to surface-located redox reactions providing a capacitive-like signature owing to their fast kinetics and reversibility [11].

Aside from the use of porous carbon materials, 3D scaffolds are of great interest since bottom-up and top-down microfabrication techniques allow for a significant improvement in the surface of the electrodes while maintaining a limited footprint area [12]. These 3D scaffolds can be combined with pseudocapacitive materials [13].

Among the various pseudocapacitive materials used for µSCs, such as ruthenium dioxide [14–16], vanadium nitride [17,18] and conducting polymers, manganese dioxide ($MnO_2$) stands out as a good compromise between availability, price and performance [19–21]. However, $MnO_2$ is known to be at a disadvantage due to low electronic conductivity. $MnO_2$ thin film deposition on 3D current collectors for µSC electrodes is thus a reasonable trade-off providing high areal capacitance and fair electronic conductivity [22].

The performance of µSCs depends not only on the choice of electrodes but also on the choice of electrolyte. The latter must possess a high ionic conductivity in order to cope with the fast redox reactions occurring in this pseudocapacitive-based µSC, as well as being able to respond to the thermal and chemical constraints. Nowadays, the electrolytes used in commercial devices are based on salts dissolved in organic solvents, owing to their wide operating potential window and good ionic conductivity,

although these are plagued by safety issues and limited thermal stability [23]. Aqueous electrolytes provide an answer to the safety concerns, showing great ionic conductivity, but they severely limit the potential window of the μSC [24] and the thermal operating range. While many μSC studies are focused on using aqueous- or organic-based liquid electrolytes, real-world implementation of these μSCs isn't feasible due to packaging issues that are liable to engender evaporation and leakage. Another packaging issue concerns the fact that the μSCs need to be integrated into a printed circuit board and must be able to withstand the reflow soldering process occurring at 250 °C.

Another possibility is the use of ionic liquids (ILs), which are presenting negligible vapor pressure and showing no degradation below ~200°C [25]. Their ionic conductivity is comparable to that of organic electrolytes and they display wide electrochemical windows, as well as excellent thermal and chemical stability [26]. However, leakage is still an issue as regards their use in μSCs.

When it comes to safety concerns, stability requirements and ease of fabrication as an electrolyte for μSCs, solid electrolytes are indeed an appealing option. Inorganic and polymer electrolytes, often employed as thin films in μBats, are not suitable for μSCs due to their very limited ionic conductivity [21]. The confinement of known liquid electrolytes presents an alternative solution: gels made from aqueous electrolytes (i.e., hydrogels) [27-29] or from ILs (i.e., ionogels) are being explored as possible μSC electrolytes. The latter display a lower ionic conductivity as compared to aqueous gels and are not subject to evaporation. Moreover, they can be operated using a wider potential window. The desirable properties that using ionogels as electrolytes for μSCs provides are a high energy density and a long lifespan for the related microdevice [30-32].

In this study, lithium and sodium salts were added in various concentrations to the chosen IL. These IL mixtures were confined following the same synthesis route that was described in a previous study [33]. The impact of the salts on confined and non-confined ILs was initially evaluated through conductivity measurements. The impact of the 3D microstructures and $MnO_2$ thin film when used as µSC electrodes was investigated by comparing these to equivalent solid-state µSCs. The IL mixtures were confined and cast onto the 3D electrodes to form solid-state $MnO_2$ // $MnO_2$ µSCs so as to study the influence of the added salts concentration. Interdigitated µSCs were then fabricated and tested at high temperatures.

## 2. Material and methods

### 2.1. Electrolyte

Lithium and sodium salts [Lithium bis(trifluoromethanesulfonyl)imide (LiTFSI) and Sodium bis(trifluoromethanesulfonyl)imide (NaTFSI), Solvionic, 99.5 % purity] were added to 1-Ethyl-3-methylimidazolium bis(trifluoromethanesulfonyl)imide (EMImTFSI) (Solvionic, 99.9 %) in different concentrations.

### 2.2. Ionogel preparation and casting

The IL electrolytes presented above were confined in polyvinylidene fluoride (PVDF Solef 6008, Solvay) matrices via non-aqueous route. The PVDF was solubilized in dimethylformamide (DMF, Acros Organics) in a concentration of 8 wt% in ambient conditions (T = 23 °C). After thorough solubilization, it was mixed with IL (ca. 83 wt% IL), in a controlled atmosphere ($H_2O$ < 0.1 ppm and $O_2$ < 0.1 ppm). After a few minutes of stirring, this precursor was then cast onto a Teflon mold or an electrode and aged until complete evaporation of the DMF solvent: the ionogel was firstly kept for 2 days

in a closed box to limit the DMF evaporation, allowing polymer unfolding and preventing cracks, and then for 2 days in an ambient atmosphere to fully evaporate the DMF. A 40-minute heat treatment at 120 °C under vacuum (0.5 mbar) was then performed in order to improve the mechanical resistance of the ionogel (completing polymer unfolding and relaxation) and the wetting of the interface between the substrate and the ionogel.

### 2.3. Conductivity measurement

The ionic conductivities were measured by electrochemical impedance spectroscopy (EIS) using Biologic-VMP3 equipment with Swagelok cells and stainless steel blocking electrodes. As concerns the non-confined IL, a Teflon ring placed in the Swagelok cell allowed for the control of the form factor (3 mm x 110 $mm^2$). For the ionogels, pellets (1 mm x 70 $mm^2$) were obtained by casting the precursor in Teflon molds which were inserted into the Swagelok cells. The frequency ranged from 1 MHz to 100 mHz with a polarization amplitude of 20 mV. The measurements were performed between -20 °C and +80 °C, every 10 °C, after the following stabilizations of the temperature: for 12 h at the initial temperature (- 20 °C) and for 2 h for each of the subsequent temperatures. All samples were dried for 12 h at 50 °C under vacuum (0.5 mbar, $H_2O$ content below 50 ppm) before taking EIS measurements. The ionic conductivity σ ($S.cm^{-1}$) was calculated from the resistance values obtained with the EIS, following the equation (1).

$$\sigma = \frac{t}{R\,S} \qquad (1)$$

Where t is the thickness of the electrolyte (cm), S the surface ($cm^2$) and R the resistance (Ω).

### 2.4. Electrode fabrication and preparation

The fabrication process of the 3D electrodes made from silicon microtubes that were used in this study has already been described in earlier works [8,13,34,35]. Briefly, the first step of this process involved using a photolithography process in order to define the geometry of the electrodes and the position of the microtubes. The silicon was then etched according to the photoresist mask by deep reactive-ion etching (DRIE). This led to the formation of microtubes providing a high surface area. Aluminum oxide ($Al_2O_3$, 100 nm) as an insulator and platinum (Pt, 40 nm) as a highly conductive current collector were then conformally deposited using the atomic layer deposition (ALD) method. The design of interdigitated electrodes was carried out by means of an additional photolithography process, followed by a plasma etching one in order to etch the platinum film and to define the interdigitated electrodes. The electrodes used in this work presented a footprint area of 4 $mm^2$. They showed an area enhancement factor (AEF) of close to 25, with the following dimensions: silicon microtubes with outer and inner diameters of 4 µm and 2 µm, respectively, and external and internal etched depths of 45 µm and 22.5 µm, respectively. This meant that an electrode with a 1 $cm^2$ footprint area had a geometric surface area of 25 $cm^2$. The $MnO_2$ pseudocapacitive layer was then conformally deposited onto the 3D electrodes using an electrodeposition route, as described elsewhere [12,33]. Prior to the deposition of $MnO_2$, the electrodes were cleaned by running 30 cyclic voltammograms (CVs) between 1.5 V and -0.35 V at 50 $mV.s^{-1}$ in a 0.1M $H_2SO_4$ solution, while using Pt as the counter electrode (CE) and Ag/AgCl as the reference electrode (RE). The $MnO_2$ film was obtained by pulsed electrodeposition in 0.1M $MnSO_4$ and in a 0.1M $H_2SO_4$ aqueous solution, under low stirring, with Pt as the CE and Ag/AgCl as the RE. Potentiostatic (1.15 V vs ref) and resting steps were alternated every 0.3 s to enhance the diffusion of $Mn^{2+}$ cations close to the Pt layer [36]. As described in earlier work, the

$MnO_2$ thin films obtained were amorphous [12]. The thickness of the deposit was tuned by the number of pulses applied (i.e., the total charge delivered to the electrode, in coulombs). In this work, the $MnO_2$ thickness was limited to ~ 450 nm via the application of 120 mC to the electrode, in order to avoid filling the spaces in and between the microtubes (**Fig. S1-S3**).

The choice of ionogel synthesis was linked to the choice of electrode materials. Indeed, one possible route of ionogel preparation, which employs formic acid, has to be avoided as it leads to $MnO_2$ dissolution.

### 2.5. Structural characterization

Scanning electron microscopy (SEM) (Merlin Zeiss) was used to determine the thickness and conformal deposition of the $MnO_2$ layer, as well as to observe the impregnation of the ionogel on the 3D electrodes.

### 2.6. Electrochemical characterization

The µSCs were characterized using CV and EIS on a VMP3-Biologic potentiostat under ambient conditions. CVs were carried out at various scan rates between 2 and 200 $mV.s^{-1}$, and between 0 and 1 V vs reference. Moreover, EIS was performed at open circuit voltage (OCV) between the frequencies of 1 MHz and 100 mHz with a voltage amplitude of 20 $mV.s^{-1}$.

The specific capacitance (C, $mF.cm^{-2}$) was evaluated from the CVs, following equation (2). This value was normalized according to the footprint area of the µSC, for the purpose of comparison with other µSC devices [37]. This normalization was based on the surface of an electrode for face-to-face µSCs, and on the surface of the full cell in the case of two interdigitated electrodes.

$$C = \frac{\int I dt}{S\,\Delta V} \qquad (2)$$

Energy density (E, J.cm$^{-2}$) and power density (P, W.cm$^{-2}$) were also calculated in order to determine the Ragone plots according the equations (3) and (4):

$$E = \frac{1}{2} C\,\Delta V^2 \qquad (3)$$

$$P = \frac{E}{\Delta t} \qquad (4)$$

Where I is the measured current (mA), t the time (s), S the surface of the µSC (cm²) and ΔV the cell voltage (V).

## 3. Results and discussion

### 3.1. Electrode and ionogel preparation

**Fig. 1a-c** shows drawings of interdigitated electrodes at different stages of the fabrication process with regard to $MnO_2$ deposition. As indicated in the zoom, the interdigitated electrodes were made from a 3D scaffold of Si / $Al_2O_3$ / Pt microtubes, that were further covered with electrodeposited $MnO_2$ film. **Fig. 1d** presents the 3D face-to-face configuration prior to the $MnO_2$ deposition.

The thickness of the $MnO_2$ deposit could be determined from SEM images of the top-view of a microtube before and after its deposition. On **Fig. 2**, the deposit, colorized in orange for the sake of clarity, shows a thickness of 450 nm. This particular deposit thickness was chosen in order to take advantage of the pseudocapacitance delivered by the $MnO_2$, without sealing the tubes and the spaces between them, thus providing access to the electrolyte.

**Fig. 3** displays ionogel pellets of 0.8 cm in diameter which were used for ionic conductivity measurements in the Swagelok cells. The ionogel was a transparent and flexible solid, despite being composed of 83 wt% IL. It did not show any leakage after ageing. When the ionogel was subjected to an annealing treatment at temperatures above room temperature, a moderate and reversible exudation of liquid (appearance of ~ 500 µm droplets on the surface) was observed due to the differential dilation of the IL and the polymer matrix [38].

The ionogel precursor was deposited on the 3D electrodes to form an 80 – 120 µm-thick thin film covering the microstructures, and enabling ionic contact between the electrodes. Partially due to the viscosity of the precursor, the spaces between the microtubes were occasionally not entirely filled by the ionogel, as observed **Fig. 4a**. The heat treatment, which was performed at 120 °C under 0.5 mbar for 40 min at the end of the ionogel ageing process.

EDX (Energy Dispersive X-Ray Analysis) measurements were also performed on microstructured electrodes covered with ionogel before and after the heat treatment (**Fig. S4**). The presence of fluorine is related to the $TFSI^-$ anion and to the PVDF matrix of the ionogel. Prior to the heat treatment, the presence of fluorine was observed from the top to the bottom of most of the microtubes, but not entirely for some of them. The filling of these empty spaces was completed thanks to the heat treatment as shown by EDX measurements (**Fig. 4b and Fig. S4**).

**Fig. 5 a-b** shows schemes of the µSCs used in this work in face-to-face and interdigitated configurations. Both devices were obtained by employing 3D silicon scaffolds as the starting point. These templates were composed using long fingers (i.e., digits, 2 mm x 100 µm). Each digit included an array of 3D silicon microtubes and was separated from other digits by a silicon wall. Two stacked films (1$^{st}$ layer = $Al_2O_3$, 2$^{nd}$

layer = Pt) were then deposited by the ALD method on the 3D silicon scaffold: (*i*) if the Pt film was etched on the top of the Si / $Al_2O_3$ wall, then two interdigitated Pt current collectors were obtained, each 3D current collector showing a footprint surface of 2 $mm^2$ (**Fig. 5 b&f**). The $MnO_2$ film was then electrodeposited onto the two interdigitated current collectors to achieve the fabrication of 3D $MnO_2$ / $MnO_2$ interdigitated µSCs; (*ii*) if no additional technological step was performed, then no electrical isolation was obtained between the fingers, thus leading to a single 3D Si / $Al_2O_3$ / Pt current collector with a footprint surface close to 4 $mm^2$. Two 3D Si / $Al_2O_3$ / Pt current collectors were then coated with $MnO_2$ films leading to the fabrication of 3D $MnO_2$ / $MnO_2$ µSCs in a face-to-face configuration (**Fig. 5 a&d**).

Face-to-face $MnO_2$ / $MnO_2$ µSCs were assembled by pressing together two 3D electrodes separated by the ionogel electrolyte. In order to limit inaccuracy due to the thickness of the electrolyte between the two electrodes, the ionogel precursor was deposited onto each electrode in a controlled volume of 60 µL.

µSCs with interdigitated $MnO_2$ / $MnO_2$ electrodes did not require an assembly process, since contact between the electrodes was already achieved through the ionogel deposition on top of the 3D electrodes.

### 3.2. Conductivity measurements on the EMImTFSI-based IL with added lithium and sodium salts

EMImTFSI is known to be a suitable electrolyte for supercapacitors due to its ionic conductivity, stability and large operating window [39]. The ionic conductivity of the non-confined IL containing different concentrations of LiTFSI or NaTFSI salts was measured in order to evaluate the impact of the additional ions. The evolution of the conductivity of these ILs at different temperatures is shown in Fig. 6a-b for added

LiTFSI and added NaTFSI, respectively. The addition of either LiTFSI or NaTFSI into the EMImTFSI produced a similar effect on the ionic conductivity.

For the EMImTFSI, it remained roughly the same overall upon the addition of 0.05M or 0.1M of LiTFSI or NaTFSI at 7.2 $mS.cm^{-1}$. On the other hand, the addition of 0.5M of LiTFSI or NaTFSI into the EMImTFSI led to a small decrease in the ionic conductivity, down to 4.6 $mS.cm^{-1}$, due to the increased viscosity.

The conductivity of a standard aqueous electrolyte (5M $LiNO_3$ in water (25.6 wt% $LiNO_3$)) used together with $MnO_2$ electrodes is displayed in **Fig. 6 a-b**. Its ionic conductivity was one decade higher than that of the IL due to a lower viscosity. The salt concentration appeared to lower the water's liquid-to-solid phase transition since no sharp decrease in the ionic conductivity, down to -20 °C, was noted. This observation was in good agreement with earlier work, showing a freezing temperature of -22.9 °C for 24.6 wt% $LiNO_3$ in water [40]. However, at higher temperatures, the water evaporation led to a decrease in and failure of the conductivity measurements above 30 °C, which did not occur for IL-based electrolytes.

The EMImTFSI presented stable behavior throughout the temperature window from -20 to +80 °C. This served to demonstrate the interest of using IL-based electrolytes over water-based electrolytes, especially when operating at temperatures higher than room temperature.

### 3.3. Conductivity measurements on the EMImTFSI-based ionogel with added lithium and sodium salts

The EMImTFSI with either LiTFSI or NaTFSI mixtures were confined in a PVDF matrix. Pellets of these ionogels were used for conductivity measurements (**Fig. 7 a** for added LiTFSI and **Fig. 7 b** for added NaTFSI). Compared to the non-confined IL (EMImTFSI

in hollow black squares), there was only a small decrease in the overall conductivity, partly due to the presence of PVDF which did not participate in the ionic conductivity. At 20 °C, the ionic conductivity of the pure EMImTFSI IL and of the ionogel was 7.2 and 3.0 $mS.cm^{-1}$, respectively. For sake of comparison, the conductivities of contemporary hydrogel electrolyte made from poly(vinyl alcohol) and LiCl are included here (**Fig. 7**), and although they show similar values, the same authors provide evidence of certain instabilities (notably, weight loss) while heating just above room temperature [41].

The differences in ionic conductivities of the ionogels, due to the variation in LiTFSI or NaTFSI concentration, showed similar trends to that of the non-confined ILs. Indeed, the conductivity decreased as the salt concentration increased, i.e., with increased viscosity. This was more noticeable for concentrations of 0.5M than it was for lower salt concentrations (0.05M and 0.1M). With 0.5M LiTFSI and NaTFSI, the ionic conductivity of the ionogel at 20 °C shifted from 3.0 $mS.cm^{-1}$ to 2.0 $mS.cm^{-1}$ and 1.15 $mS.cm^{-1}$, respectively.

The confinement, although it came with the cost of a moderate loss in ionic conductivity, helped to overcome the issue of electrolyte leakage. The addition of alkaline salts promoted the pseudocapacitive reactions occurring at the $MnO_2$ surface.

### 3.4. Evaluation of μSC performance in ionogel without alkaline salts: from planar to 3D microdevices

Face-to-face μSCs, with two 4 $mm^2$ footprint electrodes and pure EMImTFSI-based ionogel as the electrolyte, were assembled to highlight the influence of $MnO_2$ films, as well as the use of 3D microstructured electrodes. The electrodes used for the four

configurations tested were composed of planar Pt, planar Pt covered with $MnO_2$, 3D microstructured Pt and 3D microstructured Pt covered with $MnO_2$, respectively.

Prior to the deposition of the $MnO_2$ films, the influence of the 3D scaffold could be directly observed by comparing Pt-coated planar and 3D silicon wafers. An increase in intensity between the CVs (black lines and blue lines, **Fig. 8**) depicted a significant increase in current for the 3D microstructured substrate, highlighting the effect of the electrode surfaces. Indeed, the capacitance increased from 21 $\mu F.cm^{-2}$ with planar electrodes to 275 $\mu F.cm^{-2}$ with the 3D scaffold electrodes. These values correspond to the full device. Therefore, the capacitance of the corresponding Pt-coated electrodes were 42 $\mu F.cm^{-2}$ and 550 $\mu F.cm^{-2}$, respectively. This translated into an area enlargement factor (AEF) of 13, which was lower than that calculated from the geometrical improvement of the surface thanks to the 3D scaffold (AEF = 25). Although we obtained a good wetting of the electrodes with the ionogel sol precursor, the PVDF might have been positioned at the interface between the electrodes and the IL, thus blocking the access of the ions from the electrolyte to part of the $MnO_2$ active layer. It is worth noting that the capacitance of 42 $\mu F.cm^{-2}$ fitted well with previous values of double-layer capacitance reported for different metallic surfaces [42–44].

**Fig. 8** displays the CV at 20 $mV.s^{-1}$ for the µSCs assembled with planar and 3D-based electrodes (red and green, respectively) after having been covered with pseudocapacitive $MnO_2$ material. On planar electrodes, the presence of the $MnO_2$ thin film increased the capacitance of the micro-device from 21 $\mu F.cm^{-2}$ to 1800 $\mu F.cm^{-2}$, although the CV shape (red) shows a high resistivity, which may be explained in part as being due to a poor contact between the smooth Pt surface and the $MnO_2$ thin film. However, a capacitance of 1.8 $mF.cm^{-2}$ (3.6 $mF.cm^{-2}$ for a single electrode) exceeded the double layer capacitance expected for such an inorganic compound, thus

emphasizing the pseudocapacitive charge storage behavior already reported for $MnO_2$ [22,45]. Moreover, the use of $MnO_2$ on microstructured electrodes (in green) dramatically improved upon the current density attained by the other designs. The capacitance deduced from this CV was around 43 $mF.cm^{-2}$, and such a high capacitance value associated with a rectangular CV shape serves to depict the pseudocapacitive behavior of $MnO_2$ [11]. Consequently, in the case of $MnO_2$-covered electrodes, the AEF being close to 24 as measured by cyclic voltammetry fitted very well with the capacitance increase, presumably thanks to a good wetting of the $MnO_2$ surface by the ionogel. The $MnO_2$ deposited on the electrodes showed a porosity which may provide partial access to the ionogel, thus leading to higher capacitance values.

The same observations were made when using non-confined EMImTFSI as the electrolyte, as seen in **Fig. S5**.

### 3.5. Influence of alkaline salts on the performance of solid-state 3D face–to-face µSCs

A slight decrease in the ionic conductivity of the IL and of the ionogel was observed upon the addition of either lithium or sodium salts, although this addition was expected to improve the capacitive performance of µSCs based on pseudocapacitive $MnO_2$ material. Indeed, alkaline cation intercalation into the $MnO_2$ structure has been evidenced as a primary phenomenon leading to high capacitance values [46]. The ionogels, with various concentrations of LiTFSI and NaTFSI, were then used as the solid electrolyte in face–to-face µSCs with 3D electrodes covered with $MnO_2$ thin film.

CV plots of the µSCs containing LiTFSI and NaTFSI are displayed in **Fig. 9 a-b**, respectively. The increase in the redox current was linked to to the LiTFSI or NaTFSI concentration in the IL. It should be noted that with a concentration as low as 0.05M,

there were probably not enough alkaline cations in the vicinity of the electrode in order to obtain its full expected capacitance. Therefore, the capacitance still increased when the concentration of LiTFSI increased, although it reached a maximum for 0.5M. Further increases in the concentration of LiTFSI did not result in enhanced capacitance values (**Fig. S6**). The influence of added LiTFSI on the capacitance was clearly visible at low and medium scan rates (**Fig. 9 b**). At 20 $mV.s^{-1}$, the capacitance increased from 31 $mF.cm^{-2}$ to 100 $mF.cm^{-2}$ with the addition of 0.5M LiTFSI to the EMImTFSI electrolyte. This difference was still maintained at faster scan rates, even if a faster decrease in capacitance was observed in the ionogel containing 0.5M LiTFSI. It should also be noted that the lower the LiTFSI concentration, the lower the decay when fast scan rates were used (**Fig. 9 b**).

At a lower scan rate (2 $mV.s^{-1}$), the capacitance of the µSC increased up to 126 $mF.cm^{-2}$. This value compared well with that obtained on $MnO_2$-based 3D µSCs assembled in a face-to-face design, with an AEF of 65 for the 3D microstructured electrodes [35]. In the latter study, aqueous 5M $LiNO_3$ was used as the liquid electrolyte and the micro-device exhibited an increased capacitance of 650 $mF.cm^{-2}$ with a 450 nm thick $MnO_2$ active layer. This should have translated into 250 $mF.cm^{-2}$ with an AEF of 25, as per the present study. Therefore, the use of an ionogel electrolyte with 0.5M LiTFSI in EMImTFSI resulted in a 50 % decrease in performance as compared to the same µSC operated in an aqueous electrolyte. However, by using the ionogel electrolyte one is able to design an all-solid-state micro-device showing no signs of leakage or water evaporation.

The aforementioned increase in capacitance was most likely due to the presence of $Li^+$ cations showing a high mobility and contributing to the pseudocapacitive charge storage mechanism occurring at the surface of the $MnO_2$ thin films. Moreover, the

stabilization of capacitance observed while the LiTFSI concentration in the electrolyte was increased to over 0.5M, was either due to the increasing viscosity, which limited ionic conductivity, or to the restriction of $Li^+$ intercalation into the $MnO_2$. Lastly, the deposition of $MnO_2$ (120 mC over 4 $mm^2$) led to a theoretical capacity of 1.5 $C.cm^{-2}$ for a single 3D electrode. A practical capacity of 126 x 2 = 256 $mC.cm^{-2}$ was obtained for a single 3D electrode operated in ionogel electrolyte, which suggests that 17 % of the Mn sites are electrochemically active in an electrolyte of this kind. Such high electrochemical activity has never been reported before for $MnO_2$ films in ILs.

In **Fig. 9 c**, a Ragone plot depicts an increase in the energy density related to higher concentrations of LiTFSI in the electrolyte of the µSCs. As expected, according to the CVs, the energy density remained the same for a concentration of 0.5M LiTFSI. The energy density was 2.96 $\mu Wh.cm^{-2}$ with a power density of 1.07 $mW.cm^{-2}$ for a µSC with an ionogel electrolyte containing pure EMImTFSI. By way of comparison, the energy density reached 10.22 $\mu Wh.cm^{-2}$ with a power density of 1.10 $mW.cm^{-2}$ when 0.5M LiTFSI was added to the IL. This value is 3 times larger than that mentioned in our previous report concerning ionogel-based µSCs [33].

The addition of 0.5M NaTFSI to the electrolyte, instead of LiTFSI, showed similar results (**Fig. 9 d**) and led to the same observations as those for added lithium salt. As evidenced in **Fig. 9 e**, the face-to-face µSC with EMImTFSI + 0.5M NaTFSI-based ionogel as the electrolyte, displayed a capacitance of 87 $mF.cm^{-2}$ at 20 $mV.s^{-1}$. Using the same solid electrolyte, the Ragone plot (**Fig. 9 f**) shows an energy density of 9.47 $\mu Wh.cm^{-2}$ with a power density of 1.02 $mW.cm^{-2}$.

In both cases, as regards the addition of either lithium or sodium salts, a concentration of 0.5M seemed to be the best compromise between increasing the energy density and decreasing the ionic mobility due to a higher electrolyte viscosity.

In order to evidence the compatibility of these devices with high operating temperatures, CVs at different scan rates were also performed in a face–to-face configuration with pure EMImTFSI, EMImTFSI + 0.5M LiTFSI and EMImTFSI + 0.5M NaTFSI-based ionogel electrolyte µSCs at 50 and 100 °C. **Fig. 10 a** shows a decrease in the cell's resistivity with an increase in temperature. The Nyquist plots of the two other µSCs show the same evolution (**Fig. S7-S8**).

**Fig. 10 b** presents the capacitance evolution depending on the scan rates at certain temperatures for the three face-to-face µSCs with ionogel as the electrolyte. As shown beforehand in **Fig. 9**, the addition of 0.5M of LiTFSI or NaTFSI helped to improve the capacitance independently of the scan rate. The increase in temperature from room temperature to 50 °C generated an increase in capacitance for all three µSCs. However, when the scan rate was increased to a temperature of 50 °C or above, the difference in capacitance observed at a low scan rate was maintained even at 200 $mV.s^{-1}$. These µSCs were able to operate well at 100 °C, with capacitance values in the same range as those observed when cycled at 50 °C. The improved capacitance observed with added LiTFSI or NaTFSI was attributed to the intercalation of alkaline cations. This mechanism is currently under investigation using in-depth vibrational spectroscopy techniques and will be the topic of a forthcoming paper.

In terms of relaxation time $\tau_0$ (the time below which more energy is dissipated as heat than is stored [47]), a sharp decrease was observed for all 3 ionogel-based µSCs when the temperature was raised from 25 °C up to 50 °C (**Fig. 11**). It should be noted that $\tau_0$ reflects the equivalent series resistance of the micro-device and provides a clear idea of the timescale at which it can be operated in a meaningful way. The room temperature relaxation time was 7.1 s for the EMImTFSI ionogel, which was halved when increasing to 50 °C. Going up to 100 °C resulted in a $\tau_0$ of 1.7 s. Although higher

relaxation times were measured for ionogel containing LiTFSI or NaTFSI, the same trend was observed. A decrease from 10.4 s down to 5.7 s was measured for the µSC with 0.5M LiTFSI in the ionogel electrolyte when the temperature was increased from 25 °C up to 50 °C. Unlike for the pure EMImTFSI ionogel, the addition of LiTFSI or NaTFSI only resulted in a moderate decrease in $\tau_0$ when the temperature was further increased to 100 °C.

The plots of C' and C'' versus frequency, used to find the relaxation time of each device for each given temperature, are shown **Fig. S9-S11**.

Long-term cycling was also performed on face-to-face solid-state µSCs by applying galvanostatic charge / discharge cycling at 1.75 $mA.cm^{-2}$ between 0 and 1 V for 50 000 cycles. **Fig. 12** shows the evolution of the capacitance and coulombic efficiency of the two µSCs, one containing 0.5M LiTFSI and the other 0.5M NaTFSI. Both µSCs showed a similar capacitance evolution, with a slow and constant decrease starting from capacitance values of around 70 $mF.cm^{-2}$ to around 60 $mF.cm^{-2}$.

Coulombic efficiency remained constant at around 99 % and 96 % for the device containing lithium and sodium ions, respectively. These values fit well with the expected performance of supercapacitors over cycling. The difference in efficiency values between the two devices indicated a higher loss of $Na^+$ ions over $Li^+$ ions in non-reversible reactions.

### 3.6. 3D $MnO_2$ / $MnO_2$ µSCs with an interdigitated configuration

Once the most favorable salt concentrations for lithium and sodium were identified for face-to-face µSCs, further electrochemical tests were performed with interdigitated µSCs.

Solid-state 3D $MnO_2$ / $MnO_2$ interdigitated µSCs were obtained using ionogels based on pure EMImTFSI, EMImTFSI + 0.5M LiTFSI and EMImTFSI + 0.5M NaTFSI. These particular concentrations of lithium and sodium salts were chosen subsequent to an observed improvement in performance. CVs at scan rates of between 20 and 200 $mV.s^{-1}$ were performed on these interdigitated µSCs (**Fig. 13 a-c**). The addition of either lithium or sodium salts substantially and similarly enhanced the performance of the interdigitated µSCs (**Fig. 13 d**).

The same 4 $mm^2$ footprint area was used for both the face-to-face µSCs presented above, as well as the interdigitated µSCs. In the latter case, however, the surface of a single electrode was no longer 4 $mm^2$ but 2/5 of this surface (= 1.6 $mm^2$), since the two electrodes, as well as the isolation separation between them, are included in the 4 $mm^2$ footprint area. Non-interdigitated electrodes followed the same pattern as the interdigitated ones, which means that a single electrode's surface was 4/5 of the footprint area. Consequently, the reported capacitance values for the full interdigitated microdevice should be 4-fold that of a single electrode. The capacitances obtained with the interdigitated µSCs were around half the value of the corresponding capacitances with the face-to-face µSCs, which is thus in agreement with the preceding remark.

The interdigitated configuration was also noteworthy in terms of volumetric performance and device integration. Indeed, **Fig. 14** displays the capacitances normalized according to the total volume of active material in the face-to-face and interdigitated µSCs. The interdigitated configuration exhibited volumetric capacitance values that were slightly higher than those of face-to-face systems at lower scan rates. This observation served to demonstrate the interest in using interdigitated electrodes, as they provided an improved proximity between the electrodes and promoted ion

exchange. A capacitance value of 150 $F.cm^3$ at a scan rate of 20 $mV.s^{-1}$ was obtained with the interdigitated µSCs.

The face-to-face configurations used in this work had thicknesses of around 1 mm, since the thickness of the silicon-based electrodes was 400 µm and the total thickness of the ionogel electrolyte was around 200 µm. The thickness of interdigitated devices was about half that of a face-to-face ones (0.5 mm). This fact emphasized the relevance of the interdigitated configuration for a better integration into miniaturized electronic devices.

**Fig. 15** shows a Ragone plot of the two top-performing µSC configurations from this work, i.e., those using ionogel solid electrolytes and face-to-face electrodes, compared to those found in the literature [18,32,47-50]. Only ionogel-based all-solid-state µSCs are presented for comparison purposes. The review of Lethien et al. [10] reports that µSCs need energy density values superior to 100 $\mu Wh.cm^{-2}$ in order to be more versatile in terms of possible uses. This value was not reached by the µSCs presented herein, although a key issue concerning the fabrication of solid-state µSCs was addressed within the framework of this study. Nevertheless, our study clearly reveals new possibilities when it comes to improving the storage performance of solid-state µSCs, as well as for upscaling their technological fabrication process towards a pilot production line. The solid-state µSCs presented in this study do however demonstrate a competitive performance, as compared to those mentioned in other works, by reaching an energy density of between 6 and 17 $\mu Wh.cm^{-2}$.

## 4. Conclusion

The microfabrication and chemistry routes (namely, pseudocapacitive materials and ionogels) presented herein demonstrate competitive all-solid-state 3D micro-supercapacitors (μSCs), with both face-to-face and interdigitated configurations. This study required the design and tuning of the pseudocapacitive transition metal oxides, 3D microstructured electrodes and ionogel electrolytes employed. Several key issues were addressed: (*i*) the effect of $MnO_2$ as the active electrode material on the energy density of a μSC, which was shown to be a very positive one as it increases efficiency when used as a thin film on microstructured electrodes. Indeed, the capacitance obtained in this configuration was far greater than that obtained when using 2D platinum film as the electrodes; (*ii*) the ionogels used as solid electrolytes were composed of 83 wt% ionic liquids (IL) and they showed efficient, solid and flexible behavior. Owing to this composition, the ionogels were able to attain high ionic conductivity, and the addition of LiTFSI and NaTFSI salts in low concentration only resulted in a slight decrease in conductivity. The addition of alkaline salts to the IL used for synthesizing ionogels led to a substantial enhancement in the energy density of μSCs assembled with these ionogels. Although the addition of salt increases the viscosity of ILs, the cation input promoted the pseudocapacitive reactions thereby increasing the energy density delivered by the μSC; (*iii*) under operating temperatures of 50 and 100 °C, the μSCs showed an increase in overall capacitance compared to room temperature. This behavior confirmed the viability of using ionogels for all-solid-state μSCs operating at high temperatures, thus adding to the aforementioned advantages of being solid, leakage-free and flexible. Long-term galvanostatic cycling on all-solid-state face-to-face μSCs showed similar behavior upon the addition of lithium ions or sodium ions. Capacitance decreased slowly and steadily over

50 000 cycles; (*iv*) lastly, the interdigitated configuration was equivalent to regular face-to-face devices in terms of performance. This electrode design, however, provides a clear advantage in terms of cutting through the assembly process that is usually needed after electrolyte deposition.

To conclude, the combined use of 3D-designed, pseudocapacitive electrodes and ionogel solid electrolytes tuned with alkaline salts led to the fabrication of significantly improved solid-state μSCs, thereby lending to the legitimacy of the design and fabrication choices herein with a view to enhancing future solid-state μSCs in terms of both efficiency and miniaturization.

**Acknowledgments**

This study was supported by the ANR (French National Research Agency) through the DENSSCAPIO project (ANR-17-CE05-0015). The authors declare no conflict of interest. They also wish to thank the ANR STORE-EX and the French network devoted to electrochemical energy storage (RS2E) for their financial support. To the French RENATECH network, the authors would like to extend their deepest gratitude for the use of their microfabrication facilities.

**Data availability**

The raw/processed data required to reproduce these findings cannot be shared at this time as the data also forms part of an ongoing study.

**Competing interests**

The authors declare no competing interests.

## References


1. Atzori L, Iera A, Morabito G. The Internet of Things: A survey. *Computer Networks*. 2010;54(15):2787-2805. doi:10.1016/j.comnet.2010.05.010

2. Yang Y, Wang S, Zhang Y, Wang ZL. Pyroelectric Nanogenerators for Driving Wireless Sensors. *Nano Lett*. 2012;12(12):6408-6413. doi:10.1021/nl303755m

3. Zhang Y, Fang J, He C, Yan H, Wei Z, Li Y. Integrated Energy-Harvesting System by Combining the Advantages of Polymer Solar Cells and Thermoelectric Devices. *J Phys Chem C*. 2013;117(47):24685-24691. doi:10.1021/jp4044573

4. Petsagkourakis I, Tybrandt K, Crispin X, Ohkubo I, Satoh N, Mori T. Thermoelectric materials and applications for energy harvesting power generation. *Science and Technology of Advanced Materials*. 2018;19(1):836-862. doi:10.1080/14686996.2018.1530938

5. Salot R, Martin S, Oukassi S, Bedjaoui M, Ubrig J. Microbattery technology overview and associated multilayer encapsulation process. *Applied Surface Science*. 2009;256(3):S54-S57. doi:10.1016/j.apsusc.2009.09.086

6. Oudenhoven JFM, Baggetto Loïc, Notten PHL. All-Solid-State Lithium-Ion Microbatteries: A Review of Various Three-Dimensional Concepts. *Adv Energy Mater*. 2011;1(1):10-33. doi:10.1002/aenm.201000002

7. Wang Y, Liu B, Li Q, et al. Lithium and lithium ion batteries for applications in microelectronic devices: A review. *Journal of Power Sources*. 2015;286:330-345. doi:10.1016/j.jpowsour.2015.03.164

8. Létiche M, Eustache E, Freixas J, et al. Atomic Layer Deposition of Functional Layers for on Chip 3D Li-Ion All Solid State Microbattery. *Adv Energy Mater*. 2017;7:1601402. doi:10.1002/aenm.201601402

9. Conway BE. *Electrochemical Supercapacitors: Scientific Fundamentals and Technological Applications*. Springer Science & Business Media; 1999.

10. Lethien C, Le Bideau J, Brousse T. Challenges and prospects of 3D micro-supercapacitors for powering the internet of things. *Energy & Environmental Science*. 2018;12:96-115. doi:10.1039/C8EE02029A

11. Brousse T, Bélanger D, Long JW. To Be or Not To Be Pseudocapacitive? *Journal of The Electrochemical Society*. 2015;162(5):A5185-A5189. doi:10.1149/2.0201505jes

12. Eustache E, Douard C, Retoux R, Lethien C, Brousse T. $MnO_2$ Thin Films on 3D Scaffold: Microsupercapacitor Electrodes Competing with “Bulk” Carbon Electrodes. *Advanced Energy Materials*. 2015;5(18):1500680. doi:10.1002/aenm.201500680

13. Eustache E, Douard C, Demortière A, et al. High Areal Energy 3D-Interdigitated Micro-Supercapacitors in Aqueous and Ionic Liquid Electrolytes. *Advanced Materials Technologies*. 2017;2(10):1700126. doi:10.1002/admt.201700126

14. Ferris A, Garbarino S, Guay D, Pech D. 3D $RuO_2$ Microsupercapacitors with Remarkable Areal Energy. *Adv Mater*. 2015;27(42):6625-6629. doi:10.1002/adma.201503054

15. Brousse K, Pinaud S, Nguyen S, et al. Facile and Scalable Preparation of Ruthenium Oxide-Based Flexible Micro-Supercapacitors. *Adv Energy Mater*. 2020;10(6):1903136. doi:10.1002/aenm.201903136

16. Asbani B, Buvat G, Freixas J, et al. Ultra-high areal capacitance and high rate capability RuO2 thin film electrodes for 3D micro-supercapacitors. *Energy Storage Materials*. 2021;42:259-267. doi:10.1016/j.ensm.2021.07.038

17. Robert K, Stiévenard D, Deresmes D, et al. Novel insights into the charge storage mechanism in pseudocapacitive vanadium nitride thick films for high-performance on-chip micro-supercapacitors. *Energy Environ Sci*. 2020;13(3):949-957. doi:10.1039/C9EE03787J

18. Choi C, Robert K, Whang G, Roussel P, Lethien C, Dunn B. Photopatternable hydroxide ion electrolyte for solid-state micro-supercapacitors. *Joule*. 2021;5(9):2466-2478. doi:10.1016/j.joule.2021.07.003

19. Bélanger D, Brousse T, Long JW. Manganese Oxides: Battery Materials Make the Leap to Electrochemical Capacitors. *The Electrochemical Society Interface*. 2008;17(1):49-52. doi:10.1149/2.F07081IF

20. El-Kady MF, Ihns M, Li M, et al. Engineering three-dimensional hybrid supercapacitors and microsupercapacitors for high-performance integrated energy storage. *Proc Natl Acad Sci USA*. 2015;112(14):4233-4238. doi:10.1073/pnas.1420398112

21. Kyerematen NA, Brousse T, Pech D. Microsupercapacitors as miniaturized energy-storage components for on-chip electronics. *Nature Nanotechnology*. 2016;12(1):7-15. doi:10.1038/nnano.2016.196

22. Toupin M, Brousse T, Bélanger D. Charge Storage Mechanism of $MnO_2$ Electrode Used in Aqueous Electrochemical Capacitor. *Chem Mater*. 2004;16(16):3184-3190. doi:10.1021/cm049649j

23. Huang P, Pech D, Lin R, et al. On-chip micro-supercapacitors for operation in a wide temperature range. *Electrochemistry Communications*. 2013;36:53-56. doi:10.1016/j.elecom.2013.09.003

24. Long JW, Bélanger D, Brousse T, Sugimoto W, Sassin MB, Crosnier O. Asymmetric electrochemical capacitors—Stretching the limits of aqueous electrolytes. *MRS Bulletin*. 2011;36(07):513-522. doi:10.1557/mrs.2011.137

25. Wasserscheid P, Keim W. Ionic Liquids—New “Solutions” for Transition Metal Catalysis. *Angew Chem Int Ed*. 2000;39:3773-3789. doi:10.1002/1521-3773(20001103)39:21<3772::AID-ANIE3772>3.0.CO;2-5

26. MacFarlane DR, Tachikawa N, Forsyth M, et al. Energy applications of ionic liquids. *Energy Environ Sci*. 2014;7(1):232-250. doi:10.1039/C3EE42099J

27. Gao H, Lian K. Proton-conducting polymer electrolytes and their applications in solid supercapacitors: a review. *RSC Adv*. 2014;4(62):33091-33113. doi:10.1039/C4RA05151C

28. Choi C, Kim SH, Sim HJ, et al. Stretchable, Weavable Coiled Carbon Nanotube / $MnO_2$ / Polymer Fiber Solid-State Supercapacitors. *Sci. Rep.* 2015, 9387. doi:10.1038/srep09387

29. Du L, Yang P, Yu X, et al. Flexible supercapacitors based on carbon nanotube/$MnO_2$ nanotube hybrid porous films for wearable electronic devices. *J. Mater. Chem. A.* 2014; 2:17561-17567. doi:10.1039/c4ta04431b

30. Asbani B, Douard C, Brousse T, Le Bideau J. High temperature solid-state supercapacitor designed with ionogel electrolyte. *Energy Storage Materials*. 2019;21:439-445. doi:10.1016/j.ensm.2019.06.004

31. Simotwo SK, Chinnam PR, Wunder SL, Kalra V. Highly Durable, Self-Standing Solid-State Supercapacitor Based on an Ionic Liquid-Rich Ionogel and Porous Carbon Nanofiber Electrodes. *ACS Applied Materials & Interfaces*. 2017;9(39):33749-33757. doi:10.1021/acsami.7b07479

32. Rana HH, Park JH, Gund GS, at al. Highly conducting, extremely durable, hosphorylated cellulose-based ionogels for renewable flexible supercapacitors. *Energy Storage Materials.* 2020;25:70-75. doi:10.1016/j.ensm.2019.10.030

33. Asbani B, Bounor B, Robert K, et al. Reflow Soldering-Resistant Solid-State 3D Micro-Supercapacitors Based on Ionogel Electrolyte for Powering the Internet of Things. *J Electrochem Soc*. 2020;167(10):100551. doi:10.1149/1945-7111/ab9ccc

34. Eustache E, Tilmant P, Morgenroth L, et al. Silicon-Microtube Scaffold Decorated with Anatase $TiO_2$ as a Negative Electrode for a 3D Litium-Ion Microbattery. *Adv Energy Mater*. 2014;4(8):1301612. doi:10.1002/aenm.201301612

35. Bounor B, Asbani B, Douard C, Favier F, Brousse T, Lethien C. On chip MnO2-based 3D micro-supercapacitors with ultra-high areal energy density. *Energy Storage Materials*. 2021;38:520-527. doi:10.1016/j.ensm.2021.03.034

36. Bounor B. Micro-supercondensateurs 3D tout solide à électrodes hiérarchiques fabriqués à l’échelle du wafer. Published online October 23, 2019. https://www.theses.fr/2019NANT4024

37. Balducci A, Belanger D, Brousse T, Long JW, Sugimoto W. Perspective—A Guideline for Reporting Performance Metrics with Electrochemical Capacitors: From Electrode

Materials to Full Devices. *J Electrochem Soc*. 2017;164(7):A1487-A1488. doi:10.1149/2.0851707jes

38. Brachet M, Gaboriau D, Gentile P, et al. Solder-reflow resistant solid-state micro-supercapacitors based on ionogels. *J Mater Chem A*. 2016;4(30):11835-11843. doi:10.1039/C6TA03142K

39. Bonhôte P, Dias AP, Papageorgiou N, Kalyanasundaram K, Grätzel M. Hydrophobic, Highly Conductive Ambient-Temperature Molten Salts. *Inorg Chem*. 1995;35(5):1168-1178. doi:10.1021/ic951325x

40. Campbell AN, Bailey RA. The System Lithium Nitrate–Ethanol–Water And Its Component Binary Systems. *Can J Chem*. 1958;36(3):518-536. doi:10.1139/v58-074

41. Wang J, Zhan B, Zhang S, et al. Freeze-Resistant, Conductive, and Robust Eutectogels of Metal Salt-Based Deep Eutectic Solvents with Poly(vinyl alcohol). *ACS Appl. Polym. Mater.* 2022;4:2057-2064. doi:10.1021/acsapm.1c01899

42. Trasatti S. Effect of the Nature of the Metal on the Dielectric Properties of Polar Liquids at the Interface with Electrodes. A Phenomenological Approach. *J Electroanal Chem*. 1981;(123):121-139. doi:10.1016/S0022-0728(81)80047-2

43. Trasatti S. Prediction of Double Layer Parameters. The Case of Silver. *J Electroanal Chem*. 1984;172:27-48. doi:10.1016/0022-0728(84)80173-4

44. Popat PV, Hackerman N. Capacity of the Electrical Double Layer and Adsorption at Polarized Platinum Electrodes. I. Adsorption of Anions. *J Phys Chem*. 1958;62(10):1198-1203. doi:10.1021/j150568a009

45. Lee HY, Goodenough JB. Supercapacitor Behavior with KCl Electrolyte. *Journal of Solid State Chemistry*. 1999;144(1):220-223. doi:10.1006/jssc.1998.8128

46. Brousse T, Toupin M, Dugas R, Athouël L, Crosnier O, Bélanger D. Crystalline $MnO_2$ as Possible Alternatives to Amorphous Compounds in Electrochemical Supercapacitors. *Journal of The Electrochemical Society*. 2006;153(12):A2171-A2180. doi:10.1149/1.2352197

47. Taberna PL, Simon P, Fauvarque JF. Electrochemical Characteristics and Impedance Spectroscopy Studies of Carbon-Carbon Supercapacitors. *J Electrochem Soc*. 2003;150(3):A292-A300. doi:10.1149/1.1543948

48. Song D, Zare Bidoky F, Secor EB, Hersam MC, Frisbie CD. Freestanding Ion Gels for Flexible, Printed, Multifunctional Microsupercapacitors. *ACS Appl Mater Interfaces*. 2019;11(10):9947-9954. doi:10.1021/acsami.8b20766

49. El-Kady MF, Kaner RB. Scalable fabrication of high-power graphene micro-supercapacitors for flexible and on-chip energy storage. *Nat Commun*. 2013;4(1):1475. doi:10.1038/ncomms2446

50. Wang S, Hsia B, Carraro C, Maboudian R. High-performance all solid-state micro-supercapacitor based on patterned photoresist-derived porous carbon electrodes and an ionogel electrolyte. *J Mater Chem A*. 2014;2(21):7997-8002. doi:10.1039/C4TA00570H

**List of the figures and figures captions**

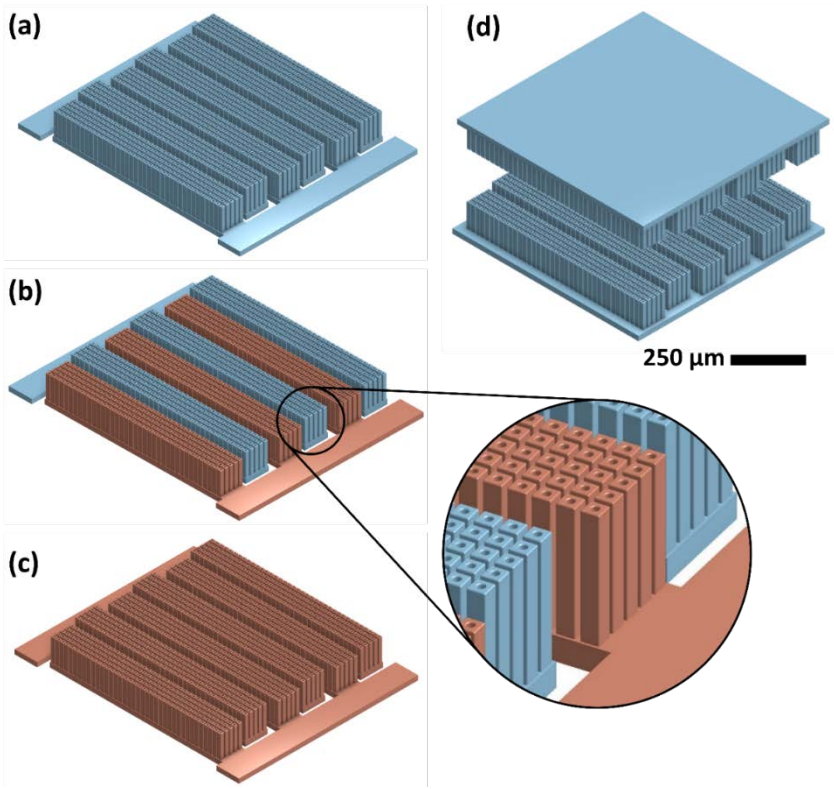


**Fig. 1 |** Simplified modeling of an interdigitated µSC with 3D electrodes made up of microtubes (footprint = 4 $mm^2$) (**a**) before $MnO_2$ deposition, (**b**) after $MnO_2$ deposition on one electrode and (**c**) after $MnO_2$ deposition on both electrodes. (**d**) Simplified design of face-to-face 3D electrodes.

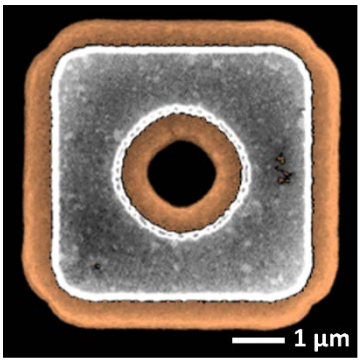


**Fig. 2 |** Superposition of SEM top-views of a micro-tube before $MnO_2$ deposition (in grey) and after (orange).

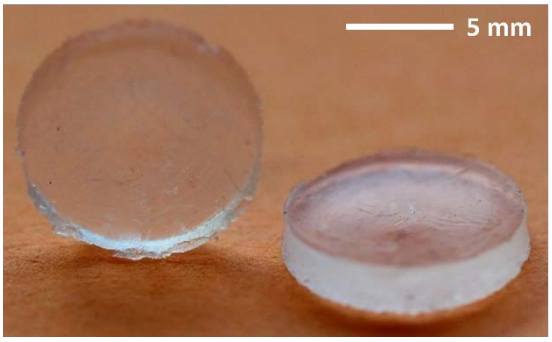


**Fig. 3 |** Ionogel pellets

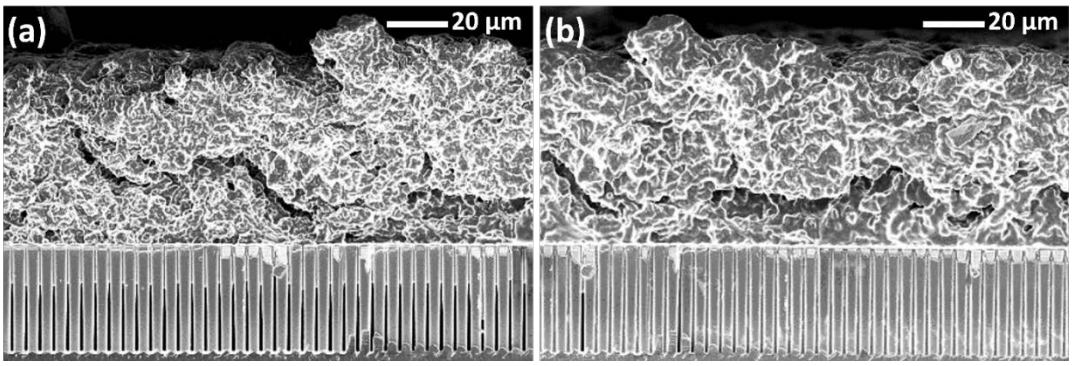


**Fig. 4 |** SEM images of a cross-section of a 3D electrode covered with ionogel showing the ionogel wetting (light grey between µtubes) of the electrodes (**a**) before the heat treatment and (**b**) after the heat treatment.

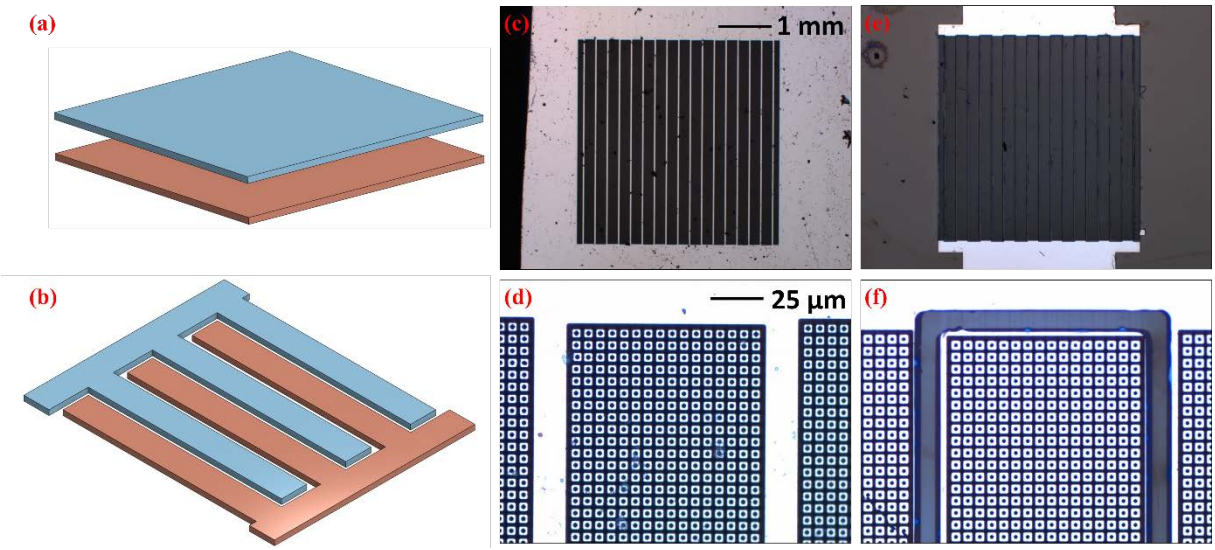


**Fig. 5 |** Two µSCs designs: two electrodes face to face (**a**) and interdigitated electrodes (**b**). Optical microscope images of a full (**c**) and a part (**d**) of the 4mm² 3D microstructured electrode used for face-to-face µSCs. Optical microscope images of a full (**e**) and a part (**f**) of the 4mm² interdigitated µSCs.

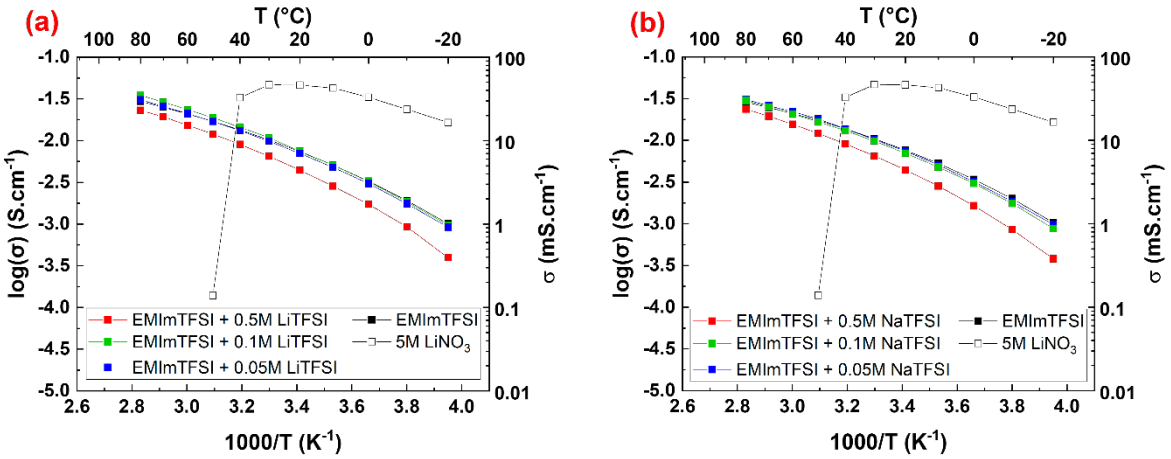


**Fig. 6 |** Conductivity vs temperature measurement of 5M $LINO_3$ and non-confined EMImTFSI with (**a**) LiTFSI added in different concentrations and (**b**) NaTFSI added in different concentrations.

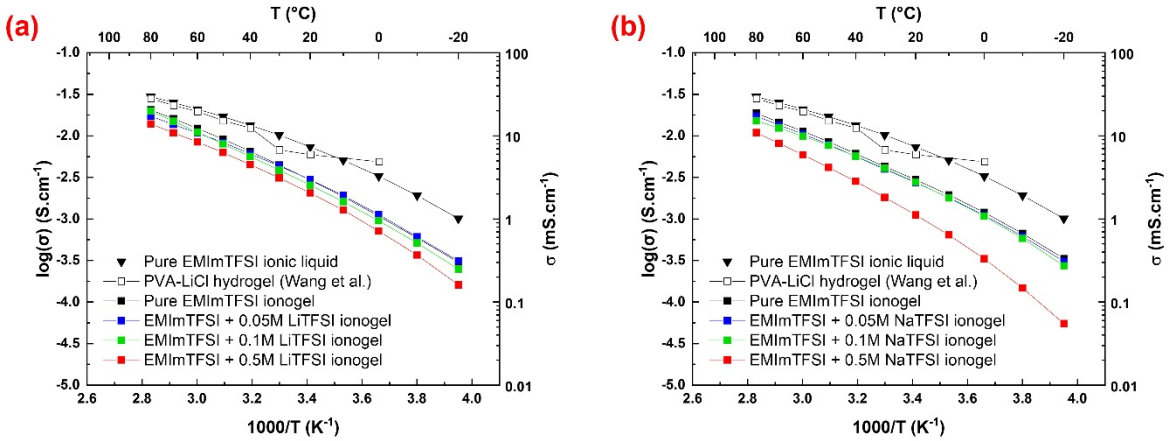


**Fig. 7 |** Conductivity vs temperature measurement of non-confined EMImTFSI and EMImTFSI based ionogels with (**a**) LiTFSI added in different concentrations and (**b**) NaTFSI added in different concentrations.

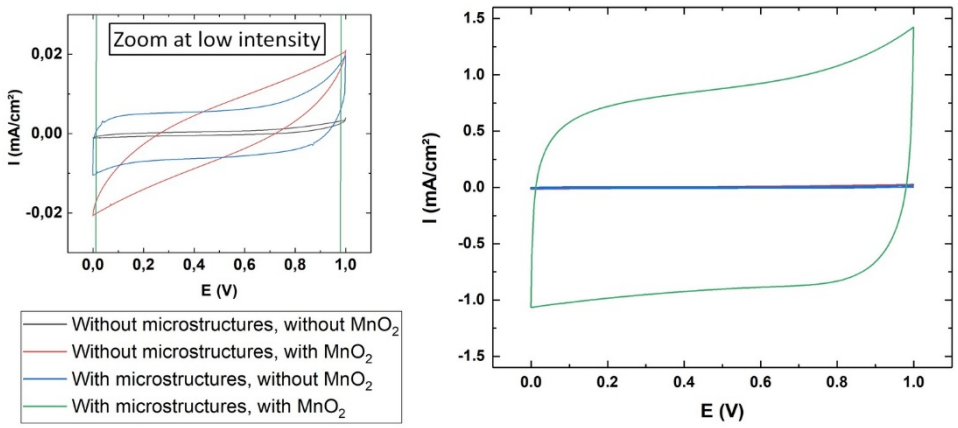


**Fig. 8 |** CVs at 20mV.$s^{-1}$ of face-to-face µSCs, with [PVDF]/EMImTFSI 17/83 wt % ionogel as electrolyte, with 3D microstructured electrodes or not and covered with $MnO_2$ or not.

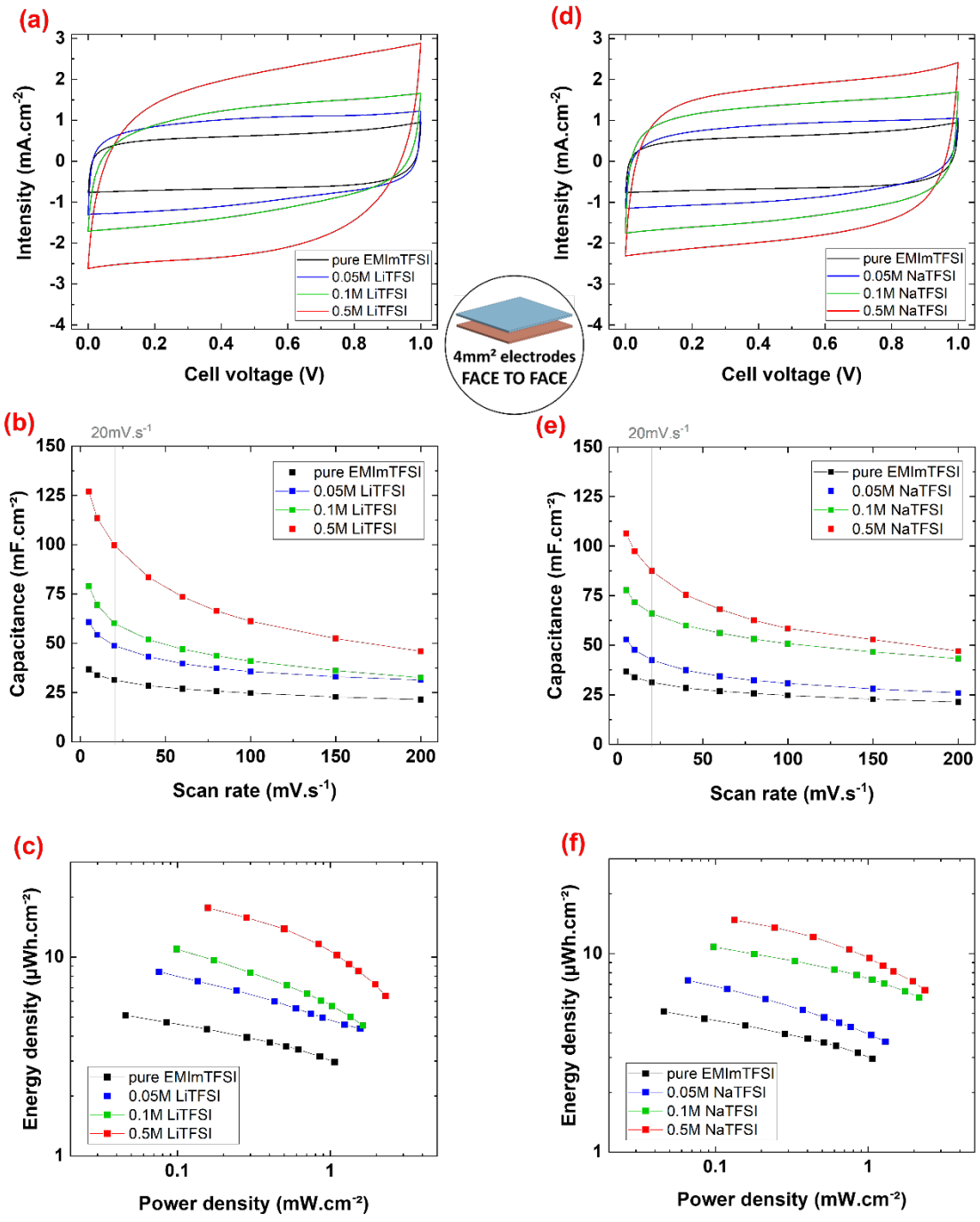


**Fig. 9 |** (**a**) CV, (**b**) capacitance vs scan rate and (**c**) Ragone plot of face-to-face µSC with ionogel electrolyte containing different concentrations of LiTFSI; (**d**) CV, (**e**) capacitance vs scan rate and (**f**) Ragone plot of face-to-face µSC with ionogel electrolyte containing different concentrations of NaTFSI.

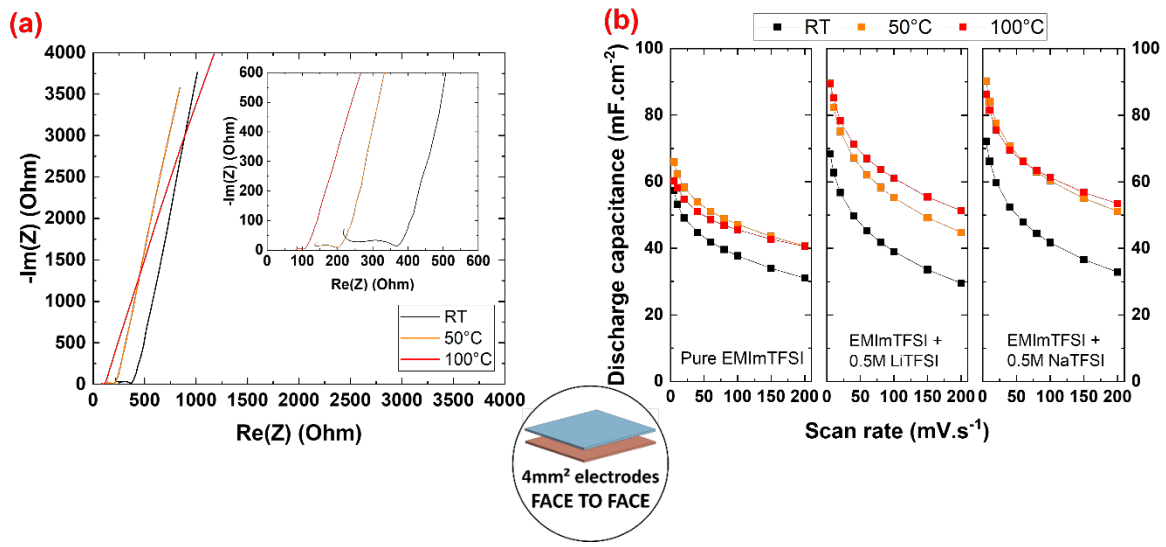


**Fig. 10 |** (**a**) Nyquist impedance at different temperatures of the µSC with [PVDF]/EMImTFSI 17/83 wt % as electrolyte and (**b**) Capacitance versus scan rate versus temperature obtained from the interdigitated µSC with ionogel electrolyte containing pure EMImTFSI, 0.5M LiTFSI in EMImTFSI and 0.5M NaTFSI in EMImTFSI.

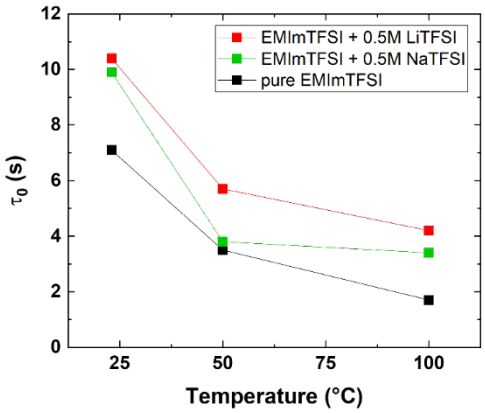


**Fig. 11 |** Time constant $\tau_0$ versus temperature of the ionogel-based μSC.

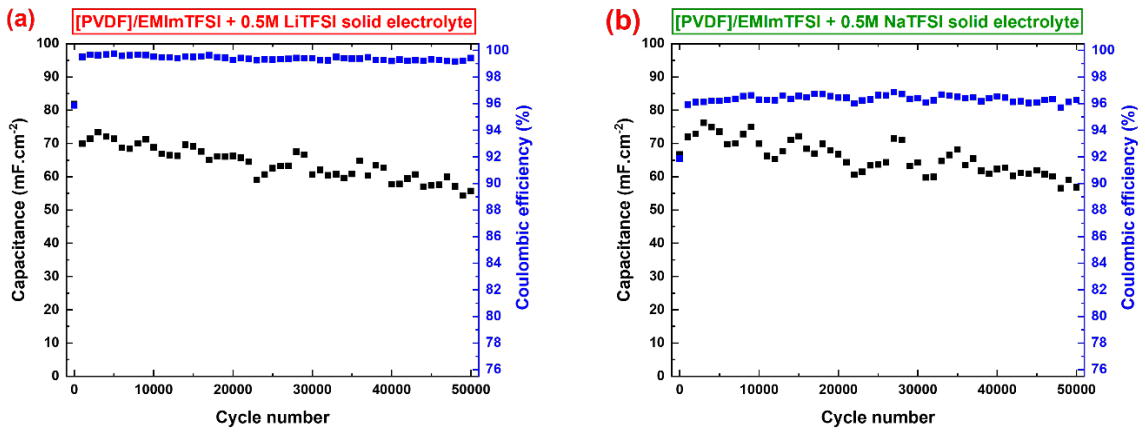


**Fig. 12 |** Evolution of the discharge capacitance and the coulombic efficiency during long term cycling of all-solid micro-supercapacitors containing (**a**) 0.5M LiTFSI and (**b**) 0.5M NaTFSI (small variations are due to days and nights temperature fluctuations.

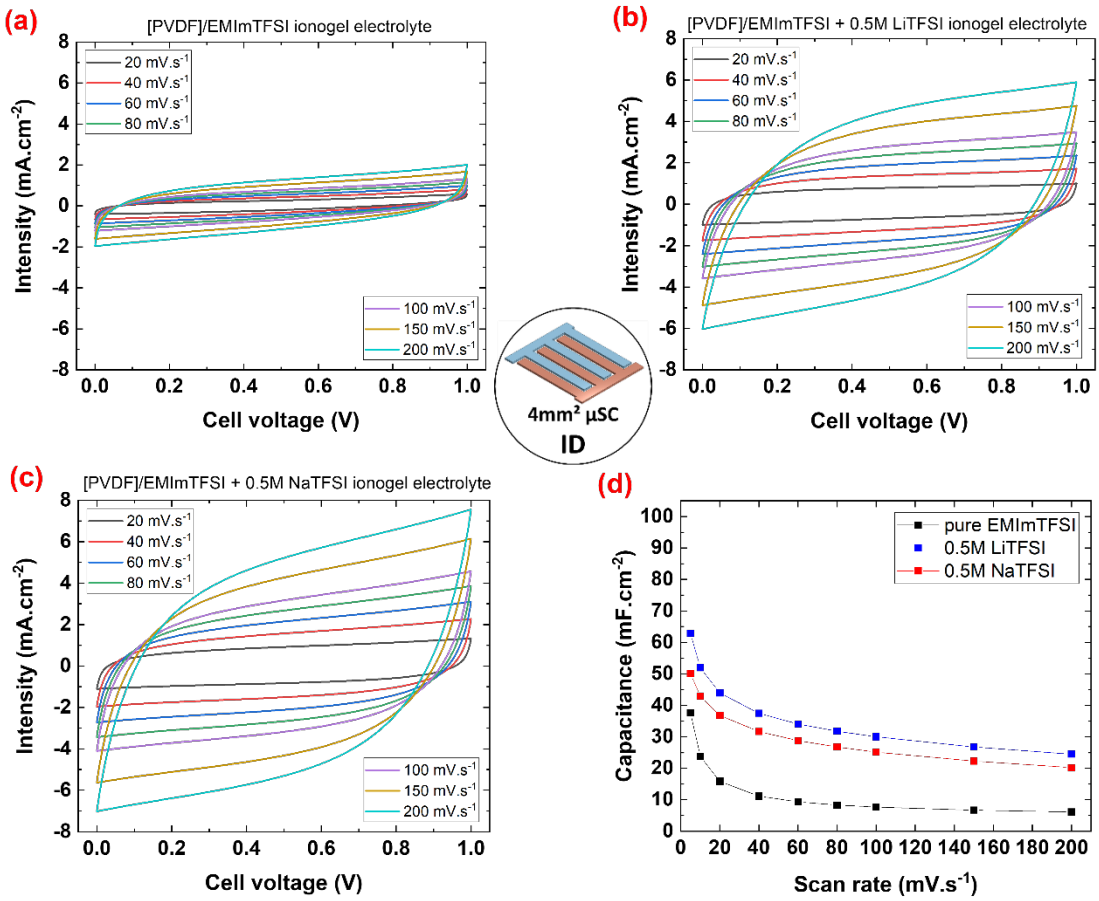


**Fig. 13 |** CVs of interdigitated µSCs with ionogel electrolyte containing (**a**) pure EMImTFSI, (**b**) EMImTFSI+0.5M LiTFSI and (**c**) EMImTFSI+0.5M NaTFSI; (**d**) Capacitance vs scan rate for the different µSCs.

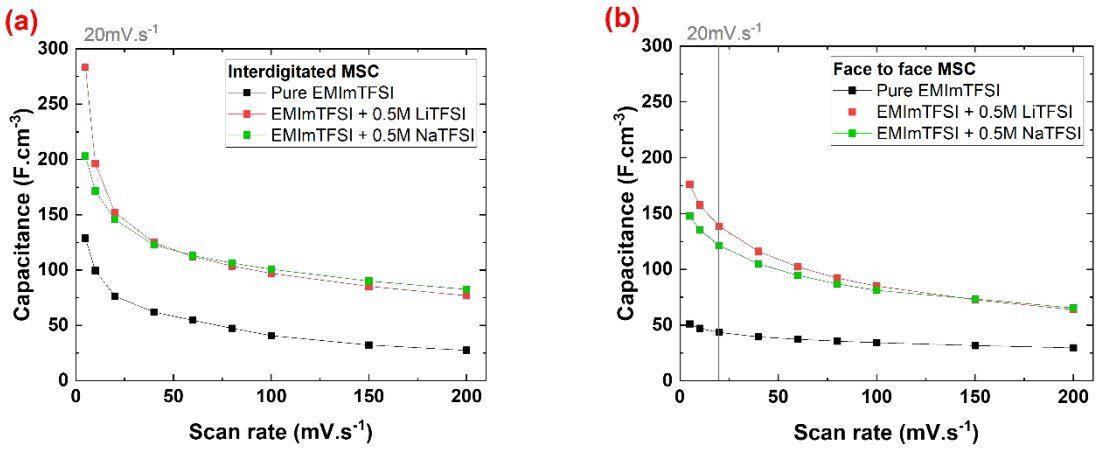


**Fig. 14 |** Capacitance normalized to µSC active material volume of all-solid (**a**) interdigitated and (**b**) face-to-face µSCs with corresponding electrolyte compositions.

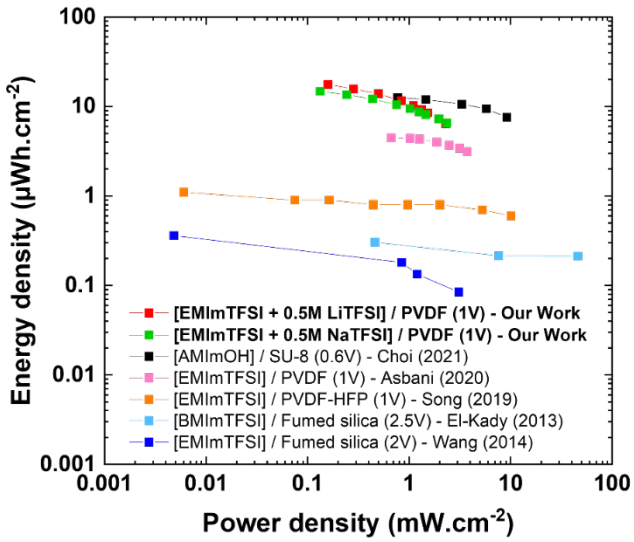


**Fig. 15 |** Ragone plot comparing our work to other ionogel-based µSCs .